Nanomanufacturing and Metrology (2023) 6:1
https://doi.org/10.1007/s41871-023-00181-x

ORIGINAL ARTICLE

Characteristics of Statically Indeterminate Symmetric Flexure Structures

Yan-Ding Qin[1] · Yue-Yang Shi[1] · Bijan Shirinzadeh[2] · Yan-Ling Tian[3] · Da-Wei Zhang[3]

Received: 11 November 2022 / Revised: 14 January 2023 / Accepted: 19 January 2023

Abstract

Statically indeterminate symmetric (SIS) flexure structures are symmetric structures with "clamped-clamped" boundary conditions. The static indeterminacy and topological symmetry significantly attenuate the parasitic motions associated with statically determinate flexure structures. Hence, SIS flexure structures feature decoupled linear and angular motions, improved motion accuracy, high stiffness, and high stability. Although SIS flexure structures have been more frequently utilized as prismatic joints, they can also be utilized as revolute joints. This study systematically investigates the characteristics of SIS flexure structures. Based on the unified compliance models of a single flexure hinge, analytical compliance models of two fundamental types of SIS flexure structures are established. In 1-degree-of-freedom or planar applications, multiple SIS-based structures can also be integrated into various configurations to transmit linear or angular motions. Corresponding stiffness models are also established. The characteristics and possible applications of the SIS flexure structures are computationally investigated through case studies. Ultimately, several SIS prototypes are manufactured, and the modeling accuracy of the established stiffness models is experimentally verified.

Highlights

1. SIS flexure structures can reduce parasitic motions and improve motion accuracy.
2. Compliance model of two SIS flexure structure are proposed.
3. Characteristics of SIS flexure structures and potential applications are analyzed.

Keywords Statically indeterminate structure · Flexure hinge · Compliance modeling · Prismatic joint

1 Introduction

Flexure hinges have been extensively utilized in precision positioning and manipulation applications [1–4] because they transmit motions through elastic deformations, which are free of friction, backlash, and wear. Generally, a flexure-based mechanism consists of multiple flexure hinges and links. Due to the significant stiffness difference between flexure hinges and links, the majority of deformations are localized within flexure hinges. Based on these characteristics, flexure hinges can be treated as flexible, and adjacent links can be treated as rigid. The behavior of a flexure hinge is highly dependent on its hinge profile. In planar flexure hinge design, common hinge profiles include circular [5, 6], elliptical [7–9], leaf-type/corner-fillet [10–12], and V-shaped [13]. Recently, more complex hinge profiles [14, 15] have also been proposed. The above flexure hinge profiles can

✉ Yan-Ding Qin
qinyd@nankai.edu.cn

Yue-Yang Shi
2120210374@nankai.edu.cn

Bijan Shirinzadeh
bijan.shirinzadeh@monash.edu

Yan-Ling Tian
meytian@tju.edu.cn

Da-Wei Zhang
medzhang@tju.edu.cn

[1] College of Artificial Intelligence, Nankai University, Tianjin, China

[2] Department of Mechanical and Aerospace Engineering, Monash University, Melbourne, Australia

[3] School of Mechanical Engineering, Tianjin University, Tianjin, China

Published online: 23 February 2023

only transmit 1-degree-of-freedom (1-DOF) motions. In some cases, multi-DOF motions are also available by incorporating several planar flexure hinges [16] or utilizing spatial flexure hinges [17].

A single flexure hinge is typically utilized as a revolute joint. However, couplings exist between the linear and angular motions, and the equivalent rotation center drifts when a lateral force is applied, resulting in motion errors. To achieve decoupled characteristics and improved motion accuracy, multiple flexure hinges can be utilized to construct certain types of flexure-based structures. For instance, parallelogram-based structures [18, 19] can be used as prismatic joints because the angular motion is eliminated through the topology. Evidently, in the literature, a class of flexure-based structures has been receiving increasing attention recently [2, 3, 20]. In such structures, both ends are clamped, and the structure is symmetric to its center. Thus, they are defined as statically indeterminate symmetric (SIS) flexure structures in this paper. The applications of SIS structures include a micropositioning stage [21] and a magnetic resonance imaging (MRI) compatible force sensor [22]. Due to the topological symmetry, couplings between linear and angular motions associated with a single hinge can be eliminated. According to the load status, SIS flexure structures can function either as prismatic or revolute joints without parasitic motions, which is investigated in this work. Due to the static indeterminacy, SIS flexure structures also feature high stiffness in in-plane and out-of-plane directions. Unlike statically determinate structures, the load-deflection relationships of SIS flexure structures are nonlinear. Fortunately, in micro/nanopositioning and manipulation applications, the motion range (generally within hundreds of microns) can be regarded as infinitesimal when compared with the structural dimension. The nonlinearities are minor and can be neglected [23].

For the compliance and stiffness of a single flexure hinge, many analytical models have been established. In general, the compliance of a flexure hinge can be obtained by utilizing beam theory [8, 9, 18, 24], empirical equation [5], or Castigliano's second theorem [10, 19]. If the aspect ratio of a flexure hinge is high (long and slender), the shear deformation can be neglected, whereas if the aspect ratio of a hinge is low (short and thick), the shear deformation needs to be taken into consideration. The modeling accuracies of the above methodologies were investigated in [25]. For a complex flexure mechanism consisting of multiple flexure hinges, the pseudo-rigid-body method is also popular [26, 27].

This work systematically investigates the characteristics of SIS flexure structures, including the unified compliance modeling of two types of SIS flexure structures and the performances of SIS-based revolute and prismatic joints. When a lateral force or moment is applied, the central link of an SIS flexure structure only experiences linear or angular deflections, thus acting as an ideal prismatic or revolute joint. In addition, the motion accuracy and stability can be improved. As the compliance modeling of a single flexure hinge has been extensively investigated, a unified shape function is adopted. The compliance models of the unified flexure hinge can be represented by four fundamental integrations, as presented in Sect. 2 and the Supplementary material. In practice, the compliance of a specific flexure hinge is available by replacing the shape function and finalizing the integration calculations of fundamental integrations. The process is straightforward, and thus it will not be pursued in this paper. Utilizing the fundamental integrations, the analytical compliance models of two fundamental types of SIS flexure structures are established in Sects. 3 and 4. Multiple SIS-based structures can also be integrated into various configurations to achieve improved performances. Ultimately, the characteristics and possible applications of the SIS flexure structure are discussed and verified through case studies and experiments, as presented in Sect. 5 and 6.

2 Unified Compliance Models and Fundamental Integrations

This study only focuses on symmetric hinge profiles where the hinge profile is symmetric to the hinge center. Some common symmetric hinge profiles are listed in Fig. 1. In this work, a unified hinge profile is adopted to establish unified compliance models applicable to all symmetric hinge profiles. The isometric projection of the unified flexure hinge is schematically illustrated in Fig. 2a, where the flexure hinge is fixed at one end and free to displace laterally and longitudinally at the other end.

A flexure hinge is a monolithic structure with an out-of-plane depth of d, a hinge length of $2l_0$, and a minimum thickness of $2t$. A coordinate is located at the hinge center. The shape function of the upper profile is denoted as $y(x)$. Because the hinge profile is symmetric, $y(x)$ is an even function. As illustrated in Fig. 2a, forces and moments are applied at the free end: three forces (F_x, F_y, and F_z) in the x-, y-, and z-axes, respectively, and two moments (M_y and M_z) with respect to the y- and z-axes, respectively. This study only focuses on the lateral deflection in the x–y and x–z planes. Because M_x does not affect the deflections in these planes, it is not considered in this study.

Due to the significant stiffness difference between the flexure hinge and adjacent link, only the flexure hinge is assumed to be flexible to facilitate compliance modeling. As illustrated in Fig. 2b, c, the linear deflections of end B in the x-, y-, and z-axes are denoted as u_B, v_B, and w_B, respectively, and the angular deflections of end B with respect to the y- and z-axes are denoted as α_{yB} and α_{zB}, respectively.

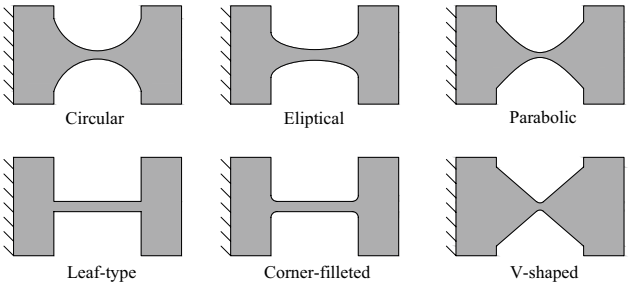

Fig. 1 Common symmetric hinge profiles

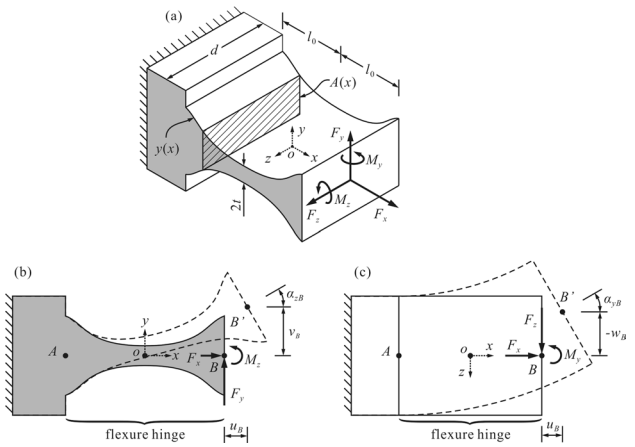

Fig. 2 **a** Isometric projection of a unified flexure hinge, **b** deflections in the *x*–*y* plane, and **c** deflections in the *x*–*z* plane

In general, there are interferences between the lateral and longitudinal deflections. The lateral loads (e.g., F_y and M_z) will cause parasitic longitudinal deflections. Meanwhile, the axial load F_x will affect the lateral deflections of the flexure hinge as it influences the inner moment of the flexure hinge [28]. However, the interferences are only obvious for extremely long and slender beams under large loads [28, 29]. As the flexure hinge is short and the loads are small in micro/nanopositioning and manipulation, the above interferences are negligible. Therefore, calculating the longitudinal, and lateral deflections independently has become common.

2.1 Longitudinal Deflection

In the longitudinal direction (*x*-axis), the linear deflection of point *B* is defined by the following equation:

$$u_B = \int_{-l_0}^{l_0} \frac{F_x}{EA(x)}\mathrm{d}x = \frac{F_x}{2Ed}\int_{-l_0}^{l_0} \frac{1}{y(x)}\mathrm{d}x = F_x P_1, \tag{1}$$

where E is the Young's modulus of the material and $A(x)$ is the cross-sectional area of the hinge at position x, as shown in Fig. 2a. $P_1 = (1/2Ed)\int_{-l_0}^{l_0}(1/y(x))\mathrm{d}x$ is defined as the first fundamental integration. It represents the effect of the material and geometric properties of the hinges.

In particular, the twist of the hinge around the *x*-axis is ignored in compliance modeling because this DOF is not utilized in most flexure hinge structures.

2.2 Lateral Deflection in the *x*–*y* Plane

In the lateral direction, Timoshenko beam theory is utilized to take the shear deformation into consideration. In the *x*–*y* plane, as illustrated in Fig. 2b, F_y and M_z cause lateral deflections. Based on the static Timoshenko beam theory, the deflections of the flexure hinge at position x without axial effects are given by the following equations:

$$\begin{cases} EI_z(x)\dfrac{\mathrm{d}\alpha_z(x)}{\mathrm{d}x} = M_z(x) \\ \dfrac{\mathrm{d}v(x)}{\mathrm{d}x} = \alpha_z(x) - \dfrac{Q_y(x)}{\kappa A(x)G}, \end{cases} \tag{2}$$

where $\alpha_z(x)$ and $v(x)$ are the angular deflection about the *z*-axis and linear deflection in the *y*-axis, respectively; $I_z(x)$ and $M_z(x)$ are the second moment of area and bending moment with respect to the *z*-axis, respectively; $Q_y(x)$ is the shear force in the *y*-axis at position x; G is the shear modulus of the material; and κ is the Timoshenko shear coefficient. For hinges with a rectangular cross section, $I_z(x) = 2\mathrm{d}y^3(x)/3$, and $\kappa = 5/6$.

Based on the static equilibrium conditions, the bending moment and shear force are obtained as follows:

$$\begin{cases} M_z(x) = M_z + F_y\left(l_0 - x\right) \\ Q_y(x) = -F_y \end{cases} \tag{3}$$

Based on Eq. (2), point *B*'s angular deflection about the *z*-axis is given by

$$\begin{aligned} \alpha_{zB} &= \int_{-l_0}^{l_0} \frac{M_z(x)}{EI_z(x)}\mathrm{d}x \\ &= \frac{3(M_z + F_y l_0)}{2Ed}\int_{-l_0}^{l_0} \frac{1}{y^3(x)}\mathrm{d}x - \underbrace{\frac{3F_y}{2Ed}\int_{-l_0}^{l_0} \frac{x}{y^3(x)}\mathrm{d}x}_{0} \\ &= \left(M_z + F_y l_0\right)P_2, \end{aligned} \tag{4}$$

where $P_2 = (3/2)\int_{-l_0}^{l_0}(1/y^3(x))\mathrm{d}x$ is defined as the second fundamental integration.

Similarly, based on Eq. (2), point *B*'s linear deflection in *y*-axis is defined by

$$
\begin{aligned}
v_B &= \int_{-l_0}^{l_0} \alpha_z(x)\mathrm{d}x - \int_{-l_0}^{l_0} \frac{Q_y(x)}{\kappa GA(x)}\mathrm{d}x \\
&= x\alpha_z(x)\|_{-l_0}^{l_0} - \int_{-l_0}^{l_0} x\mathrm{d}(\alpha_z(x)) + \frac{F_y}{2\kappa Gd}\int_{-l_0}^{l_0}\frac{1}{y(x)}\mathrm{d}x \\
&= l_0\alpha_{zB} - \int_{-l_0}^{l_0}\frac{xM_z(x)}{EI_z(x)}\mathrm{d}x + F_y\Omega P_1 \\
&= l_0\alpha_{zB} + \frac{3F_y}{2Ed}\int_{-l_0}^{l_0}\frac{x^2}{y^3(x)}\mathrm{d}x + F_y\Omega P_1 \\
&= l_0\left(M_z + F_y l_0\right)P_2 + F_y P_3 + F_y\Omega P_1,
\end{aligned}
\tag{5}
$$

where $P_3 = (3/2Ed)\int_{-l_0}^{l_0}(x^2/y^3(x))\mathrm{d}x$ is defined as the third fundamental integration. And $\Omega = E/(\kappa G)$ which represents the properties of the material.

In summary, Eqs. (4) and (5) can be rewritten in a matrix form as follows:

$$
\begin{aligned}
\begin{bmatrix} v_B \\ \alpha_{zB} \end{bmatrix} &= \begin{bmatrix} \Omega P_1 + l_0^2 P_2 + P_3 & l_0 P_2 \\ l_0 P_2 & P_2 \end{bmatrix}\begin{bmatrix} F_y \\ M_z \end{bmatrix} \\
&= \boldsymbol{C}_{xy}\begin{bmatrix} F_y \\ M_z \end{bmatrix},
\end{aligned}
\tag{6}
$$

where matrix $\boldsymbol{C}_{xy}$ is defined as the lateral compliance matrix of the flexure hinge in the x–y plane.

2.3 Lateral Deflections in the x–z Plane

The lateral deflections of the flexure hinge in the x–z plane are depicted in Fig. 2c. Unlike those in Fig. 2b, the lateral deflections in the x–z plane represent the flexure hinge's out-of-plane stiffness, which needs to be high to improve the stability and load capacity. Based on the static equilibrium conditions, the bending moment and shear force relationships at position x can be written as

$$
\begin{cases} M_y(x) = M_y - F_z\left(l_0 - x\right) \\ Q_z(x) = F_z, \end{cases}
\tag{7}
$$

where $M_y(x)$ is the bending moment with respect to the y-axis and $Q_z(x)$ is the shear force in the z-axis.

The same method presented in Sect. 2.2 can be utilized to obtain the lateral deflections in the x–z plane. The process is straightforward, and thus it is omitted for the conciseness of the paper. Point B's angular and linear deflections in the x–z plane are given in the following equations:

$$
\alpha_{yB} = \frac{6(M_y - F_z l_0)}{Ed^3}\int_{-l_0}^{l_0}\frac{1}{y(x)}\mathrm{d}x = (M_y - F_z l_0)\frac{12P_1}{d^2},
\tag{8}
$$

$$
\begin{aligned}
-w_B &= l_0\alpha_{yB} - \frac{6F_z}{Ed^3}\int_{-l_0}^{l_0}\frac{x^2}{y(x)}\mathrm{d}x - \frac{F_z}{2\kappa Gd}\int_{-l_0}^{l_0}\frac{1}{y(x)}\mathrm{d}x \\
&= \left(M_y - F_z l_0\right)\frac{12l_0P_1}{d^2} - F_z P_4 - F_z\Omega P_1,
\end{aligned}
\tag{9}
$$

where $P_4 = (6/Ed^3)\int_{-l_0}^{l_0}(x^2/y(x))\mathrm{d}x$ is defined as the fourth fundamental integration. As Fig. 2c illustrates, the sign difference between α_{yB} and w_B must be noted.

In summary, Eqs. (8) and (9) can also be rewritten in a matrix form:

$$
\begin{aligned}
\begin{bmatrix} w_B \\ \alpha_{yB} \end{bmatrix} &= \begin{bmatrix} (\Omega + \frac{12l_0^2}{d^2})P_1 + P_4 & \frac{-12l_0}{d^2}P_1 \\ \frac{-12l_0}{d^2}P_1 & \frac{12}{d^2}P_1 \end{bmatrix}\begin{bmatrix} F_z \\ M_y \end{bmatrix} \\
&= \boldsymbol{C}_{xz}\begin{bmatrix} F_z \\ M_y \end{bmatrix},
\end{aligned}
\tag{10}
$$

where matrix $\boldsymbol{C}_{xz}$ is defined as the lateral compliance matrix of the flexure hinge in the x–z plane.

In particular, Eqs. (1), (6), and (10) represent unified compliance models. For a given hinge profile, one only needs to substitute the specific shape function and finalize the integrations of P_1–P_4. Thus, these integrations are defined as the fundamental integrations of a hinge profile. The calculations of these fundamental integrations are purely mathematical, and thus they will not be pursued herein. However, the exact expressions for the fundamental integrations of some common profiles are provided in the Supplementary material.

A single flexure hinge is frequently utilized as a revolute joint to transmit angular motions about the z-axis. In this case, the angular compliance with respect to the z-axis (i.e., α_{zB}/M_z) should be high, whereas the longitudinal and out-of-plane compliance should be low to suppress all the off-axis motions. However, Eq. (6) reveals a disadvantage of a single flexure hinge: the equivalent rotation center drifts when a lateral force is applied [12, 13]. Taking the lateral compliance matrix $\boldsymbol{C}_{xy}$ as an example, the difference between $C_{xy}(1,1)$ and $C_{xy}(2,1)$ indicates that the drift of the equivalent rotation center causes an additional linear compliance of $\Omega P_1 + P_3$ at point B. This inevitable motion error is undesirable in ultra-precision applications. In practice, multiple flexure hinges can be combined in various configurations to improve motion accuracy, such as parallelogram structures [2, 19]. However, these parallelogram-based structures can only transmit linear motions. In the literature, SIS flexure structures have been widely utilized [2, 3, 7]. From the structural point of view, these SIS flexure structures can be classified into two fundamental types, which will be systematically investigated in the subsequent sections.

3 SIS Flexure Structure Type I

Figure 3a depicts the schematic diagram of the SIS flexure structure type I (hereafter denoted as SIS-I). A central link is connected to the fixed boundary through two identical flexure hinges. A coordinate is located at the center point of the central link, and the same external loads as in Fig. 2a are applied at point *O*. Compared with a single flexure hinge, the distinct characteristics of SIS-I include very high stiffness and improved motion accuracy. Theoretically, due to the topological symmetry, if a lateral force or moment is applied, the central link will only experience linear or angular deflections, functioning as an ideal prismatic or revolute joint.

In the longitudinal direction, SIS-I is equivalent to two flexure hinges connected in parallel. As a result, the longitudinal compliance will be reduced by half. Based on Eq. (1), the longitudinal deflection is given below:

$$u_O = F_x P_1/2 \tag{11}$$

As both ends are clamped, axial tension is inevitable when lateral loads are applied, resulting in a nonlinear load-deflection relationship. Based on our previous research [23], the nonlinearity is obvious only when the deformations are large. In practice, the motion range of a flexure-based mechanism is generally on the micron scale, and the nonlinearity caused by the axial tension is negligible [29]. Based on the above assumption, the loads and reactions in the *x*–*y* and *x*–*z* planes are illustrated in Fig. 3b, c, respectively. As the axial tension is neglected, SIS-I can be treated as a linear system, and the boundary condition of SIS-I can be regarded as a "clamped slide" during the lateral compliance modeling. In addition, linear superposition can be utilized to facilitate compliance modeling.

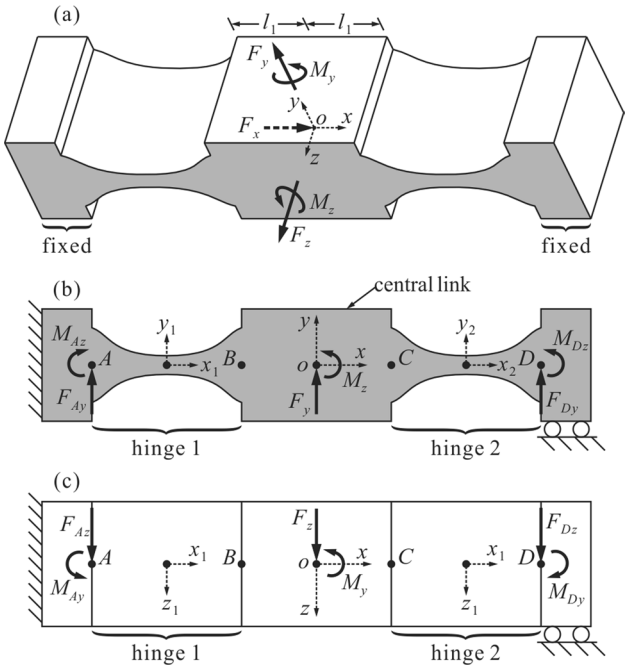

Fig. 3 SIS flexure structure type I (SIS-I): **a** schematic diagram, **b** loads and reactions in the *x*–*y* plane, and **c** loads and reactions in the *x*–*z* plane

3.1 Lateral Deflections in the *x*–*y* Plane

In the *x*–*y* plane, based on the static equilibrium conditions, the following equations are obtained:

$$\begin{cases} F_y + F_{Ay} + F_{Dy} = 0 \\ M_z - M_{Az} + M_{Dz} - (F_{Ay} - F_{Dy})(2l_0 + l_1) = 0 \end{cases} \tag{12}$$

As there are four unknown variables, this type of structure is statically indeterminate to the second degree. The reactions of SIS-I can be solved using the flexibility method. The flexibility method involves removing the constraints from point *D* and treating the reactions F_{Dy} and M_{Dz} as additional loads. This transformation results in a statically determinate structure. Based on the compatibility equations, the transformed structure should satisfy the following boundary conditions at point *D*:

$$v_D = 0, \alpha_{zD} = 0 \tag{13}$$

Based on Eq. (6), the lateral deflections of the transformed structure can be obtained using the linear superposition method. The process is straightforward, and the following equations are obtained:

$$\begin{bmatrix} v_D \\ \alpha_{zD} \end{bmatrix} = \overbrace{\begin{bmatrix} 1 & 2(l_0+l_1) \\ 0 & 1 \end{bmatrix} \boldsymbol{C}_{xy} \begin{bmatrix} F_y + F_{Dy} \\ M_{A1} \end{bmatrix}}^{\text{hinge 1}} + \overbrace{\boldsymbol{C}_{xy} \begin{bmatrix} F_{Dy} \\ M_{Dz} \end{bmatrix}}^{\text{hinge 2}}, \tag{14}$$

where $M_{A1} = M_z + M_{Dz} + F_y l_1 + 2F_{Dv}(l_0 + l_1)$.

Combining Eqs. (12)–(14), the reactions in the *x*–*y* plane are calculated to be

$$\begin{cases} F_{Ay} = -\frac{1}{2}F_y + \frac{a_1}{2b_1}M_z \\ F_{Dy} = -\frac{1}{2}F_y - \frac{a_1}{2b_1}M_z \\ M_{Az} = \frac{l_0}{2}F_y + \frac{a_1 - b_1(2l_0+l_1)}{2b_1}M_z \\ M_{Dz} = \frac{l_0}{2}F_y - \frac{a_1 - b_1(2l_0+l_1)}{2b_1}M_z, \end{cases} \tag{15}$$

where $a_1 = (l_0 + l_1)P_2, b_1 = \Omega P_1 + (l_0 + l_1)^2 P_2 + P_3$.

Subsequently, the linear and angular deflections of the central link are given below:

$$\begin{bmatrix} v_O \\ \alpha_{zO} \end{bmatrix} = \begin{bmatrix} 1 & l_1 \\ 0 & 1 \end{bmatrix} \boldsymbol{C}_{xy} \begin{bmatrix} F_y + F_{Dy} \\ M_{A1} \end{bmatrix} = \frac{\Omega P_1 + P_3}{2b_1} \begin{bmatrix} b_1 & 0 \\ 0 & P_2 \end{bmatrix} \begin{bmatrix} F_y \\ M_z \end{bmatrix} \tag{16}$$

Comparing Eq. (16) with Eq. (6), the linear and angular compliances in the x–y plane are significantly reduced, resulting in a very high stiffness. As the central link is assumed to be rigid, the parameter l_1 has no influence on the linear compliance in the y-axis. Due to the topological symmetry, there are no off-diagonal quantities in Eq. (16). As a result, SIS-I can function as a prismatic joint [30] or revolute joint [31].

Figure 4a depicts the schematic diagram of a prismatic joint (half of SIS-I). When F_y is applied, SIS-I is equivalent to two replicates of this prismatic joint connected in parallel. An example of using the SIS-I structure as a prismatic joint is the micropositioning stage in [21]. Figure 5a illustrates the schematic diagram of a revolute joint (half of SIS-I). Its application can be found in the MRI-compatible force sensor in [22]. When M_z is applied, SIS-I is equivalent to two replicates of this revolute joint connected symmetrically about the z-axis. Thus, the two equivalent structures can be treated as the building blocks of SIS-I. As they are only half of SIS-I, their corresponding linear and angular compliances are twice that of SIS-I. Based on the reciprocal relationship between compliance and stiffness, the linear stiffness of the prismatic joint in Fig. 4a is derived from Eq. (16) and given below:

$$k_p = \frac{F_y}{v_O} = \frac{1}{\Omega P_1 + P_3} \tag{17}$$

Similarly, the angular stiffness of the revolute joint in Fig. 5a is derived:

$$k_\alpha = \frac{M_z}{\alpha_{zO}} = \frac{b_1}{(\Omega P_1 + P_3) P_2} \tag{18}$$

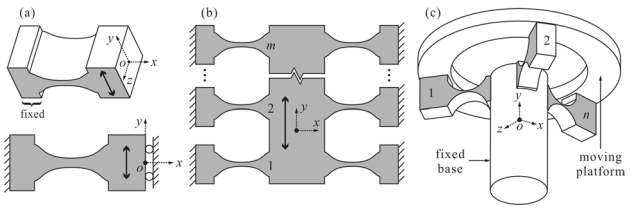

Fig. 4 **a** Equivalent structure of SIS-I under a force in the y-axis, **b** prismatic joint through a linear combination along the y-axis, and **c** prismatic joint through a symmetric combination about the y-axis

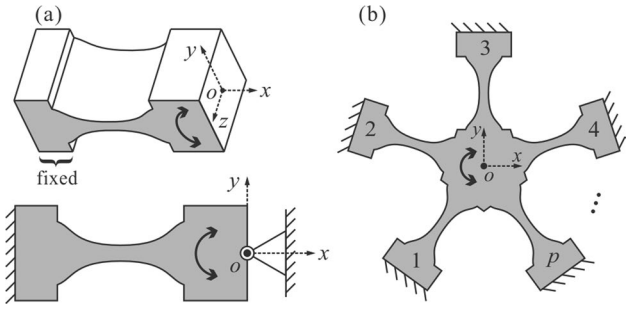

Fig. 5 **a** Equivalent structure of SIS-I under a moment about the z-axis and **b** revolute joint through a symmetric combination about the z-axis

When a prismatic joint is desired, multiple SIS-I-based structures can be cascaded linearly along the y-axis [19] or symmetrically about the y-axis [32], as illustrated in Fig. 4b, c, respectively. In Fig. 4b, each replicate can be identical or different, whereas the replicates in Fig. 4c should be identical. Compared with the basic SIS-I in Fig. 3, if $m > 1$ and $n > 2$, the angular stiffness will be significantly improved, suppressing the unwanted rotations. Based on Eq. (17), the corresponding linear stiffness of the prismatic joints in Fig. 4b, c are given in the following equations:

$$\begin{cases} [k_p]_m = 2(k_{p1} + k_{p2} + \ldots + k_{pm}), & m \geq 1 \\ [k_p]_n = n \cdot k_p, & n \geq 2 \end{cases}, \tag{19}$$

where m and n are the numbers of replicates, as shown in Fig. 4b, c, respectively.

When a revolute joint is desired, p identical replicates can be arranged symmetrically about the z-axis, as illustrated in Fig. 5b. In this case, if $p > 2$, the linear motions will be significantly attenuated. Based on Eq. (18), the angular stiffness is expressed as follows:

$$[k_r]_p = p \cdot k_r, \quad p \geq 2 \tag{20}$$

3.2 Lateral Deflections in the *x*–*z* Plane

The loads and reactions in the x–z plane are shown in Fig. 3c. The following equations are derived from the static equilibrium conditions:

$$\begin{cases} F_z + F_{Az} + F_{Dz} = 0 \\ M_y + M_{Ay} - M_{Dy} + (F_{Az} - F_{Dz})(2l_0 + l_1) = 0 \end{cases} \tag{21}$$

Similar to Sect. 3.1, to solve the statically indeterminate problem, the constraints are removed from point D, and the following equations are obtained from the compatibility equations:

$$\begin{bmatrix} w_D \\ \alpha_{yD} \end{bmatrix} = \overbrace{\begin{bmatrix} 1 & -2(l_0+l_1) \\ 0 & 1 \end{bmatrix} \boldsymbol{C}_{xz} \begin{bmatrix} F_z + F_{Dz} \\ M_{A2} \end{bmatrix}}^{\text{hinge 1}} + \overbrace{\boldsymbol{C}_{xz} \begin{bmatrix} F_{Dz} \\ -M_{Dy} \end{bmatrix}}^{\text{hinge 2}} = \begin{bmatrix} 0 \\ 0 \end{bmatrix} \tag{22}$$

where $M_{A2} = M_y - M_{Dy} - F_z l_1 - 2F_{Dz}(l_0 + l_1)$. Combining Eqs. (21) and (22), the reactions in the x–z plane are calculated to be

$$\begin{cases} F_{Az} = -\frac{1}{2}F_z - \frac{a_2}{b_2}M_y \\ F_{Dz} = -\frac{1}{2}F_z + \frac{a_2}{b_2}M_y \\ M_{Ay} = \frac{l_0}{2}F_z - \frac{b_2 - 2a_2(2l_0+l_1)}{b_2}M_y \\ M_{Dy} = \frac{l_0}{2}F_z + \frac{b_2 - 2a_2(2l_0+l_1)}{b_2}M_y \end{cases} \tag{23}$$

where $a_2 = 6(l_0 + l_1)P_1, b_2 = \left[\Omega d^2 + 12(l_0 + l_1)^2\right]P_1 + d^2 P_4$. Subsequently, the linear and angular deflections of the central link are derived:

$$\begin{aligned} \begin{bmatrix} w_O \\ \alpha_{yo} \end{bmatrix} &= \begin{bmatrix} 1 & -l_1 \\ 0 & 1 \end{bmatrix} \boldsymbol{C}_{xz} \begin{bmatrix} F_z + F_{Dz} \\ M_2 \end{bmatrix} \\ &= \frac{\Omega P_1 + P_4}{2} \begin{bmatrix} 1 & 0 \\ 0 & \frac{12P_1}{b_2} \end{bmatrix} \begin{bmatrix} F_z \\ M_y \end{bmatrix} \end{aligned} \tag{24}$$

For SIS-I, its linear compliance in the y-axis and angular compliance about the z-axis are the DOFs, and thus low stiffness is required in the two directions. On the contrary, SIS-I's compliances in the other directions are the degrees of constraints, so high stiffness is preferred in these directions. Equations (11), (16), and (24) provide analytical compliance models of SIS-I, and thus they can be utilized to facilitate the design and optimization.

3.3 Computational Investigations

The linear compliance in the y-axis and the angular compliance about the z-axis are investigated. The two most widely utilized hinge profiles are adopted: right circular and leaf-type profiles. As listed in the Supplementary material, the fundamental integrations of the right circular profile can be derived from those of the elliptical profile by letting $\epsilon = \gamma = 1$ and introducing $R = b = a$ (the radius of the circular arc). Similarly, the fundamental integrations of the leaf-type profile can be derived from those of the corner-filleted profile with $R = 0$. For flexure hinges, the modeling accuracy is highly dependent on the geometric parameters, as reported in [25]. Therefore, it is necessary to evaluate the modeling accuracy of the established compliance models across the variation ranges of the geometric parameters. The variation ranges are listed in Table 1, which form the design space for SIS-I. Hence, a specific SIS-I can be represented by a design point in the design space. A non-dimensional parameter $\beta = t/b$ is introduced to characterize the aspect ratio of the right circular profile. Similarly, a non-dimensional parameter $\gamma = t/l_0$ is introduced for the leaf-type profile.

Finite element analysis (FEA) is carried out to obtain the SIS-I compliance across the design space. The material is assumed to be an aluminum alloy with a Young's modulus of 72 GPa, a density of 2.7×10^3 kg/m^3, a Poisson's ratio of 0.3, and a yield strength of 434 MPa. The FEA models for the two profiles are illustrated in Fig. 6a, and 7a, respectively. Each FEA model is clamped at both ends, and lateral loads are exerted at the center point of the central link. The flexure hinge is meshed with fine grids, and the elements are aligned to the shape of the hinge to improve accuracy. To guarantee the resultant deformations with a small deflection range, a lateral force of 10 N and a lateral moment of 1 Nm are adopted to derive the linear compliance in the y-axis and angular compliance with respect to the z-axis, respectively. Subsequently, the modeling error is defined as the relative difference between the analytical and FEA results.

Response surface methodology (RSM) [33] using a three-factor five-level central composite design is adopted to analyze the modeling error across the design space. Only 15 design points are required using RSM, and the relationships between the modeling error and geometric parameters can be represented by a quadratic equation.

The computational results for SIS-I with the right circular profile are presented in Fig. 6b, c. The modeling error for the linear compliance is between − 9.63% and 9.16%. The largest modeling errors occurs at $R = 7.29$ mm, $\beta = 0.03, l_1 = 15$ mm. The influence of the non-dimensional geometric parameter β is significant because the modeling errors of the fundamental integrations are highly dependent on β, as reported in [25]. During analytical modeling, the central link is assumed to be rigid. As a result, the linear compliance of the central link is not taken into consideration in Eq. (16). However, the central link is flexible, and its compliance (although small compared to that of the hinge) will also increase the modeling error. Compared with β, the influences of R and l_1 are moderate. The modeling error of the angular compliance is between − 9.75% and 16.79%. The largest modeling error occurs at $R = 9$ mm, $\beta = 0.05$, and $l_1 = 15.71$ mm. In the error plot, the modeling error of the angular compliance is clearly sensitive to all the geometric parameters.

The computational results for SIS-I with the leaf-type profile are presented in Fig. 7b, c. For linear compliance, the modeling error is between − 10.92% and 6.88%. The largest modeling error occurs at $l_0 = 3$ mm, $\gamma = 0.03$, and

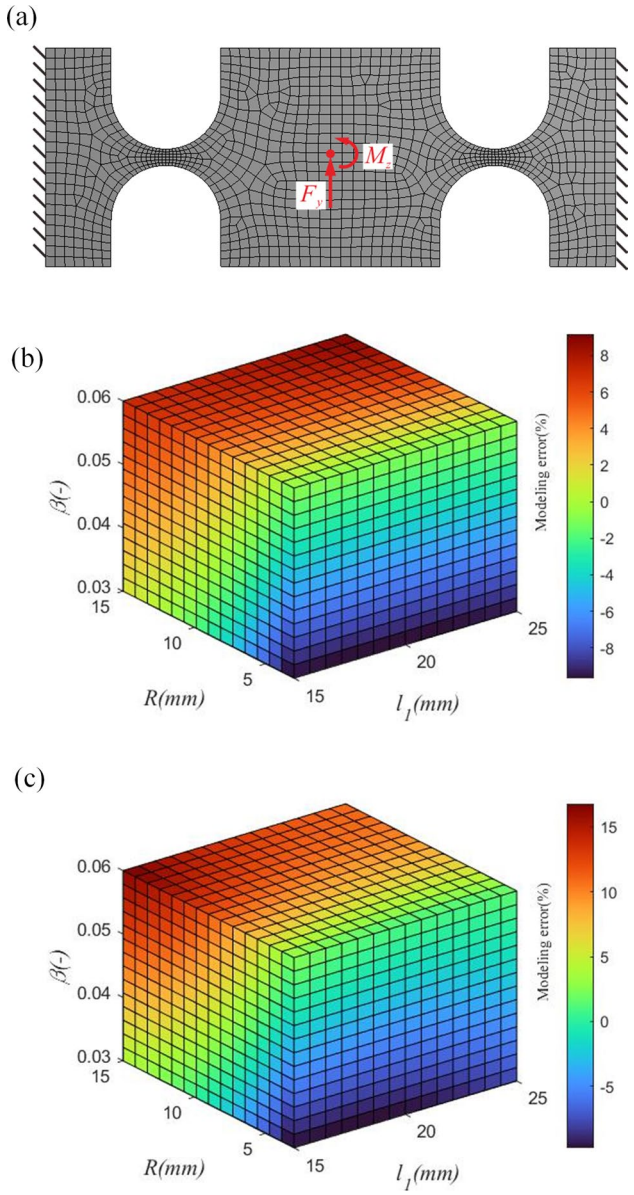

Fig. 6 SIS-I with a right circular profile: **a** FEA model, **b** modeling error of the linear compliance, and **c** modeling error of the angular compliance

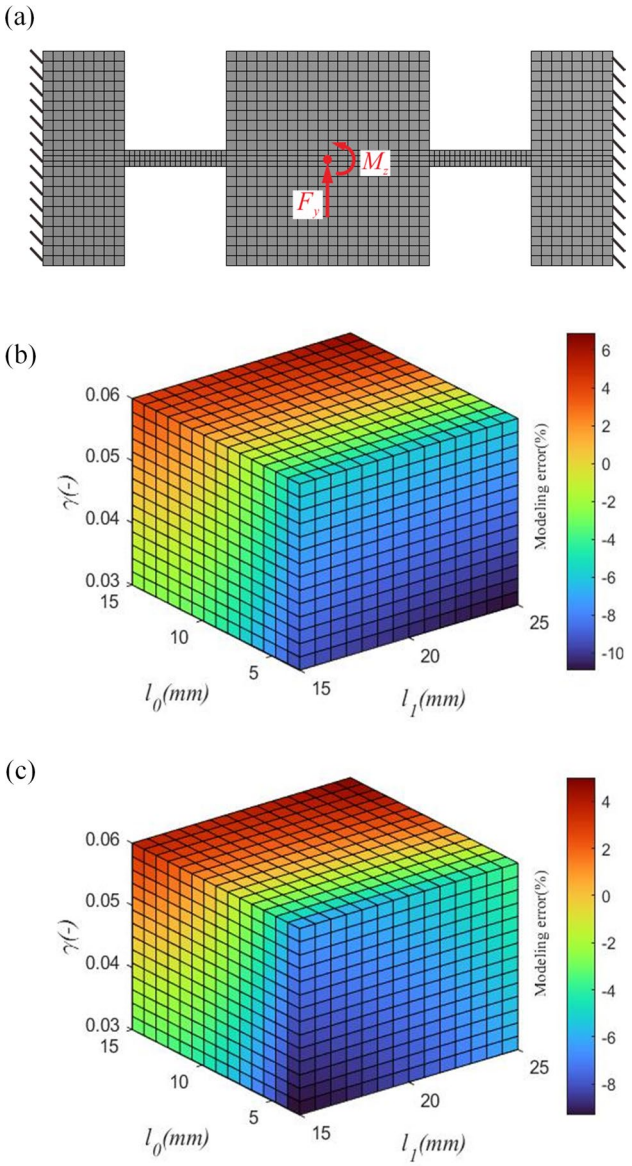

Fig. 7 SIS-I with a leaf-type profile: **a** FEA model, **b** modeling error of the linear compliance, and **c** modeling error of the angular compliance

Table 1 Variation ranges of the parameters

Right circular	Range	Leaf-type	Range
R (mm)	3–15	l_0 (mm)	3–15
β (–)	0.03–0.06	γ (–)	0.03–0.06
l_1 (mm)	15–25	l_1 (mm)	15–25
d (mm)	10	d (mm)	10

$l_1 = 25$ mm. For angular compliance, the modeling error is between − 9.31% and 5.01%. The largest modeling error occurs at $l_0 = 3$ mm, $\gamma = 0.03$, and $l_1 = 15$ mm. Similar to the right circular profile, when l_0 is large, the analytical model will overestimate the linear and angular compliance. In addition, the relationships between the modeling error and geometric parameters are similar for the linear and angular compliances. The modeling errors are sensitive to l_0 and γ, whereas the influence of l_1 is not obvious. This outcome is reasonable as the stiffness difference between the flexure hinge and central link is more significant in the leaf-type profile than in a right circular profile with the same hinge length and minimum thickness. Thus, the influence of the central link can be reduced in leaf-type profiles.

For a given SIS-I with right circular or leaf-type profiles, Figs. 6 and 7 can be utilized as a reference to estimate the modeling error of the linear and angular compliances.

4 SIS Flexure Structure Type II

In practice, a second type of SIS flexure structure (SIS-II) has also been proposed [20, 34], and the fundamental structure can be schematically illustrated in Fig. 8a. The planar compliance of SIS-II with elliptical hinge profiles has been systematically investigated in our previous work [23]. Unlike SIS-I, in SIS-II, the central link is connected to two arms and then to the fixed boundary through four identical flexure hinges. As two flexure hinges are used in each arm, the stiffness can be maintained at a reasonable level. However, the relatively large size may affect the structural compactness.

As illustrated in Fig. 8a, a coordinate is located at the center point of the central link. Same as Fig. 3a, external loads are applied at point O. The additional geometric parameters of SIS-II are also illustrated in Fig. 8a, i.e., the arm length l_1 and central link length $2l_2$. The loads and reactions in the x–y and x–z planes are presented in Fig. 8b, c, respectively. The same method in Sect. 3 is utilized to solve the statically indeterminate problem and obtain the resultant deflections of SIS-II. The process is straightforward and thus omitted for the conciseness of this paper. The deflections of SIS-II are given below:

$$u_O = F_x P_1 \tag{25}$$

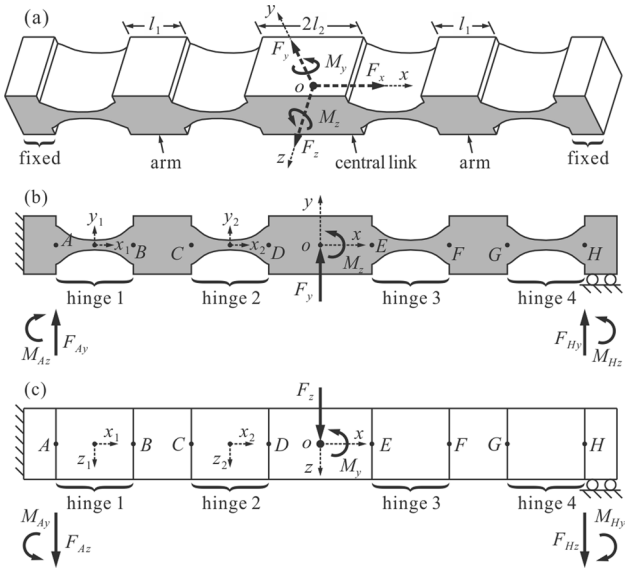

Fig. 8 SIS flexure structure type II (SIS-II): **a** schematic diagram, **b** loads and reactions in the x–y plane, and **c** loads and reactions in the x–z plane

$$\begin{bmatrix} v_O \\ \alpha_{zO} \end{bmatrix} = \begin{bmatrix} b_3/4 & 0 \\ 0 & \frac{P_2}{b_3+(4l_0+l_1+2l_2)^2 P_2} \end{bmatrix} \begin{bmatrix} F_y \\ M_z \end{bmatrix}, \tag{26}$$

where $b_3 = 4RP_1 + (2l_0 + l_1)^2 P_2 + 4P_3$.

$$\begin{bmatrix} w_O \\ \alpha_{yO} \end{bmatrix} = \frac{b_4}{d^2} \begin{bmatrix} 1 & 0 \\ 0 & \frac{12P_1}{b_4+3(4l_0+l_1+l_2)^2 P_1} \end{bmatrix} \begin{bmatrix} F_z \\ M_y \end{bmatrix}, \tag{27}$$

where $b_4 = \left[\Omega d^2 + 3\left(2l_0 + l_1\right)^2\right] P_1 + d^2 P_4$.

Same as SIS-I, the couplings between the linear and angular motions are eliminated. Hence, SIS-II can also be utilized as a prismatic or revolute joint according to the load status. Similar to Fig. 5, multiple SIS-II-based structures can also be arranged using the same configurations, such as the examples presented in [23]. The corresponding linear and angular stiffness can be obtained following the same method in Eqs. (17)–(20). The process is straightforward and will not be shown herein.

5 Case Studies

5.1 SIS-Based Revolute Joints

Although SIS flexure structures are frequently utilized as prismatic joints in flexure-based mechanism designs, they can also be utilized as revolute joints, as evident from Sects. 3 and 4. To verify this, a flexure-based lever mechanism is adopted as an example to investigate the characteristics of SIS-based revolute joints.

The schematic diagram of a lever mechanism is shown in Fig. 9, where point O is the rotation center of the lever, point A is the input point, and point B is the output point. Figure 9a, b illustrate two common revolute joints (dashed-outlined part). In Fig. 9a, a single flexure hinge is arranged orthogonal to the actuation direction [35], and in Fig. 9b, a single flexure hinge is arranged parallel to the actuation direction [3]. For the two revolute joints, the angular stiffness is the same, whereas the orientation of the flexure hinge is different. For comparison, two SIS-based revolute joints are also illustrated in Fig. 9c, d. As outlined in Sects. 3 and 4, the angular stiffness is increased in both SIS-based revolute joints, and SIS-I in Fig. 9c has the highest angular stiffness. In Fig. 9b–d, only the corresponding revolute joint is depicted, as the other parts of the lever mechanism remain unchanged. Therefore, the characteristics of SIS-based revolute joints can be investigated by comparing the performances of the revolute joints.

The lever mechanism is assumed to be a monolithic structure with an out-of-plane depth of $d = 10$ mm. For simplicity

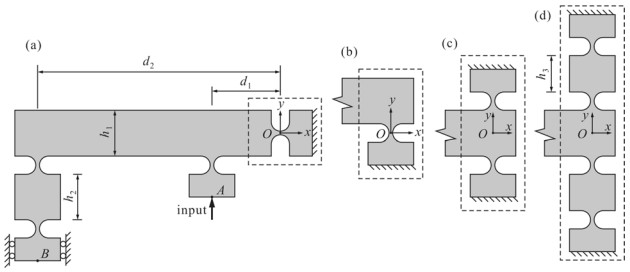

Fig. 9 Lever mechanism with different revolute joints: **a** single flexure hinge orthogonal to actuation, **b** single flexure hinge parallel to actuation, **c** SIS-I, and **d** SIS-II

Table 2 Performances of the revolute joints

	(a)	(b)	(c)	(d)
DAR	3.963	3.988	3.742	3.981
Input stiffness (N/μm)	0.0843	0.0618	5.241	0.158
Maximum stress (MPa)	0.476	0.349	2.267	0.621
Resonant frequency (Hz)	30.44	24.14	263.4	44.39

and without loss of generality, the other geometric parameters of the lever mechanism are manually assigned. All the right circular flexure hinges are assumed to be identical with $R = 6$ mm and $\beta = 0.1$. The other geometric parameters are defined in Fig. 9. Their values are manually assigned as follows: $h_1 = 30$ mm, $h_2 = 40$ mm, $h_3 = 30$ mm, $d_1 = 40$ mm, and $d_2 = 160$ mm. Thus, the lever mechanism has a theoretical displacement amplification ratio (DAR) of 4. The material is assumed to be the same aluminum alloy as presented in Sect. 3.3. For the static characteristics, a displacement input of 1 μm is applied to drive point A, and the following parameters are derived: DAR, input stiffness, and maximum stress. For the dynamic characteristics, modal analyses are performed, and the first natural frequencies are recorded. As this section focuses on the lever mechanism's in-plane behavior, the out-of-plane modes are neglected. The computational analyses are carried out, and the results are provided in Table 2.

The DAR is an important index of the lever mechanism. Due to the slight drift of the rotation center and lever compliance, the theoretical DAR is difficult to reach. The computational results show that the DAR is the lowest for SIS-I, whereas the DARs of the other revolute joints are very close to each other.

For the revolute joints in Fig. 9a, b, the orientation difference affects the performances. Figure 9a achieves a higher input stiffness, higher maximum stress, and higher resonant frequency. For the SIS-based revolute joints in Fig. 9c and d, because the angular stiffness is higher than a single flexure hinge, the input stiffness, maximum stress, and resonant frequency can be increased, especially for SIS-I. Compared

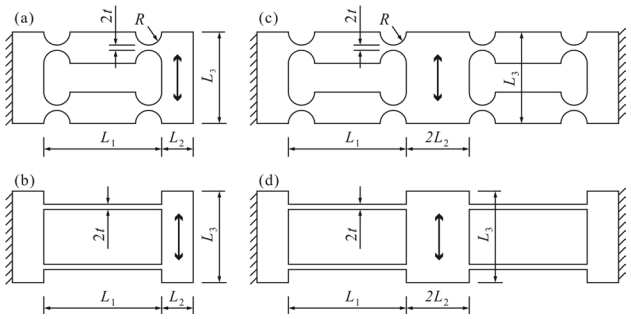

Fig. 10 Flexure-based prismatic joints: **a** right circular hinge parallelogram, **b** leaf parallelogram, **c** SIS-II with a right circular profile, and **d** SIS-I with a leaf-type profile

Table 3 Geometric parameters of the prismatic joints

R (mm)	t (mm)	d (mm)	L_1 (mm)	L_2 (mm)	L_3 (mm)
5	0.25	100	50	15	20

with SIS-II, the very high angular stiffness of SIS-I leads to the highest resonant frequency and most severe stress concentration. This condition makes SIS-I appropriate in high-frequency applications, while the motion range will be limited due to the severe stress concentration.

5.2 SIS-Based Prismatic Joints

Prismatic joints are important components in micro/nanomanipulation mechanisms. Several statically indeterminate prismatic joints are presented in Fig. 10. Hinge and leaf parallelograms are presented in Fig. 10a, b. They are common prismatic joints and are statically indeterminate to the first degree. SIS-II with a right circular profile and SIS-I with a leaf-type profile are presented in Fig. 10c, d.

The geometric parameters are listed in Table 3, and computational analyses are carried out to investigate the performances of the prismatic joints. The material is assumed to be the same aluminum alloy as presented in Sect. 3.3. During the computational analyses, a displacement input of 100 μm is applied. The parasitic motions, in-plane and out-of-plane stiffness, and first natural frequency are investigated. The results are shown in Table 4.

As shown in Table 4, for the hinge parallelogram and leaf parallelogram, the parasitic translations are at the level of 0.1% with respect to the primary motion, and the parasitic rotations are on the order of microradians. For 1-DOF applications, these parasitic motions will be impossible to compensate for and will affect the motion accuracy. On the contrary, parasitic motions can be attenuated over 1000 times in SIS-based prismatic joints. Small-magnitude parasitic motions are negligible.

Table 4 Summary of the computational results

	Hinge	SIS-II	Leaf	SIS-I
Parasitic translation in x-axis (nm)	− 91.63	− 0.0085	− 111.31	− 0.0097
Parasitic rotation about z-axis (μrad)	4.26	0.0041	1.57	0.00033
In-plane stiffness (N/μm)	0.0576	0.116	0.0114	0.0231
Out-of-plane stiffness (N/μm)	0.38	3.49	0.12	1.62
First natural frequency (Hz)	250.86	251.28	129.72	129.85

Table 5 Geometric parameters and modeling error for each hinge

	1	2	3	4	5	6	7	8	9
β (–)	0.03	0.03	0.03	0.04	0.04	0.04	0.05	0.05	0.05
l_0/R (–)	0.5	0.75	1	0.5	0.75	1	0.5	0.75	1
Analytical stiffness (N/μm)	4.78	4.42	4.34	7.59	6.80	6.64	10.9	9.51	9.21
Measured stiffness (N/μm)	4.27	4.80	4.23	7.27	6.55	6.03	9.50	8.64	8.52
Error (%)	10.6	− 8.64	2.63	4.14	3.70	9.15	12.94	9.18	7.51

The in-plane stiffness of SIS-II and SIS-I are approximately twice those of the parallelograms in Fig. 10a, b, respectively. However, the out-of-plane stiffness has been increased by approximately ten times. This condition can help improve the stability and load capacity. SIS-based prismatic joints show slight improvements from their parallelogram-based counterparts in terms of the first natural frequency.

6 Experimental Studies

To validate the proposed compliance models, a series of SIS-I flexure hinge prototypes are manufactured, and the linear stiffness along the y-axis is measured. For simplicity, circular flexure hinges are adopted, and the design spaces are defined as $\beta = 0.03$–0.05, $l_0/R = 0.5$–1, and R is fixed to 10 mm.

These hinges are made of 6061 aluminum alloy and are manufactured via wire electrical discharge machining. The diameter of the cutting wire is 0.2 mm, and the cutting speed is 10 mm/min. The manufacturing tolerance of the hinges is approximately 0.02 mm. The experiment setup is shown in Fig. 11. This experiment is carried out on a manual tension-compression testing machine (HLD, HANDPI, China). The SIS prototypes are clamped on the clip of the testing machine. A hook is attached to the flexure hinge and is connected to a force gauge (SN-100N, HANDPI, China). The force gauge is fixed on the moving platform of the tension-compression testing machine. The displacement of the flexure hinge is sensed by an eddy current displacement sensor (ML33-2 mm-00-08, MIRAN, China). Nine SIS-I prototypes are manufactured and tested. The geometric parameters of the hinges are listed in Table 5.

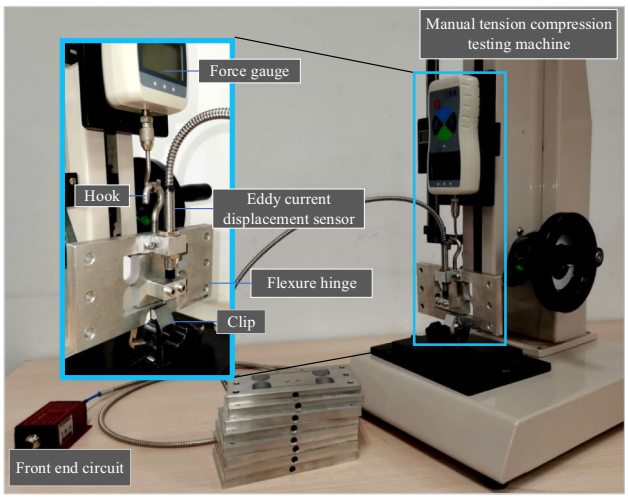

Fig. 11 Experimental setup for stiffness testing

During the experiments, each hinge is first clamped along the y-axis and then pulled by the force gauge. A force-displacement data pair is recorded when the sensors' readings are stable. Several data pairs are collected for each hinge, and linear regression is used to derive the displacement-force relationship of each hinge. The stiffness is the slope of the force-displacement relationship. The experiment data are given in the Supplementary material. The analytical stiffness is given in Eq. (17).

The modeling errors are listed in Table 5. The modeling error is between − 8.64% and 12.94%. Similar to the simulation results of the right circular hinges, the influence of the non-dimensional geometric parameter β is obvious. Besides the model itself, the manufacturing and assembling errors also contribute to the overall error, and the accuracy of the model is considered acceptable.

Table 6 Analysis of variance of the experiment

	SS	*df*	MS	*F*	*P*
Intercept	291.613	1	291.613	9.193	0.039
β	104.337	2	52.169	1.645	0.301
l_0/R	94.178	2	47.089	1.484	0.329
Error	126.891	4	31.723		
Total	617.019	9			

The analysis of variance results is given in Table 6. The SS, df, and MS columns represent the residual sum of square, DOFs, and mean sum of the square residual of each factor, respectively, and the F and P columns are the F statistics and probability of the F-test of each factor, respectively. In the table, the P values of parameters β and R/l_0 are greater than 0.05, which means random factors, such as the manufacturing and assembling errors, are important sources of the discrepancy between the analytical and experimental results. Nevertheless, the geometrical parameter β has a smaller P value than R/l_0, which indicates that it has a more significant influence on the modeling error than R/l_0.

7 Conclusions

This paper systematically describes the characteristics of a class of SIS flexure structures. Two fundamental types of SIS flexure structures, namely, SIS-I and SIS-II, are proposed and investigated. Unified analytical compliance models for the SIS flexure structures are established and verified through computational analyses and experiments. Because the established models are unified, the fundamental integrations of some common hinge profiles are provided in the Supplementary material. Therefore, the compliance models established in this paper are readily applicable to a wide range of applications.

Due to the static indeterminacy and topological symmetry, SIS flexure structures feature decoupled linear and angular motions, improved motion accuracy, high stiffness in the in-plane and out-of-plane directions, and high stability. These characteristics make SIS flexure structures attractive in ultra-precision positioning and manipulation tasks. In practice, SIS flexure structures are frequently utilized as prismatic joints. However, this paper reveals that they can also be utilized as revolute joints. According to the expected functionality in transmitting linear or angular motions, multiple SIS-based structures can be combined in various configurations for outstanding performance. The corresponding compliance models for these SIS-based structures are also established in this study. In future work, the nonlinear behavior of SIS flexure structures will be further investigated. In addition, the integration and application of SIS flexure structures in micro/nanomanipulators will be investigated.

Supplementary Information The online version contains supplementary material available at https://doi.org/10.1007/s41871-023-00181-x.

Acknowledgements Not applicable.

Author contributions YDQ was in charge of the whole research and wrote the manuscript; YYS conducted the experiments and wrote the manuscript; BS assisted with theoretic modeling and manuscript revision; YLT and DWZ assisted with finite elementary analysis and laboratory analyses. All authors read and approved the final manuscript.

Funding This research was funded by the National Natural Science Foundation of China under Grants 61873133, and 52005270; and in part by the Natural Science Foundation of Tianjin under Grant 21JCZDJC00090.

Availability of data and materials Not applicable.

Declarations

Competing interests The authors have no competing interests to declare that are relevant to the content of this article.

References

1. Das TK, Shirinzadeh B, Ghafarian M, Al-Jodah A, Zhong Y, Smith J (2020) Design, analysis and experimental investigations of a high precision flexure-based microgripper for micro/nano manipulation. Mechatronics 69:66
2. Zhang Z, Yan P, Hao GB (2017) A large range flexure-based servo system supporting precision additive manufacturing. Engineering 3(5):708–715
3. Watanabe S, Ando T (2017) High-speed xyz-nanopositioner for scanning ion conductance microscopy. Appl Phys Lett 111(11):4
4. Gao Q, He M, Lu X, Zhang C, Cheng T (2019) Simple and high-performance stick-slip piezoelectric actuator based on an asymmetrical flexure hinge driving mechanism. J Intell Mater Syst Struct 30(14):2125–2134
5. Yan WX, Liu JH, Guan EG, Yan N, Zhao YZ (2017) Force transmission of flexure-based leverage mechanism for static unbalance measuring system under self-gravity effect. Adv Mech Eng 9(11):14
6. Cheng T, He M, Li H, Lu X, Zhao H, Gao H (2017) A novel trapezoid-type stick-slip piezoelectric linear actuator using right

circular flexure hinge mechanism. IEEE Trans Ind Electron 64(7):5545–5552
7. Smith ST, Badami VG, Dale JS, Xu Y (1997) Elliptical flexure hinges. Rev Sci Instrum 68(3):1474–1483
8. Wei H, Shirinzadeh B, Tang H, Niu X (2021) Closed-form compliance equations for elliptic-revolute notch type multiple-axis flexure hinges. Mech Mach Theory 156:104154
9. Wei H, Yang J, Wu F, Niu X, Shirinzadeh B (2022) Analytical modelling and experiments for hybrid multiaxis flexure hinges. Precis Eng 76:294–304
10. Chen N, Tian C (2021) Design, modeling and testing of a 3-dof flexible piezoelectric thin sheet nanopositioner. Sens Actuators A Phys 323:9
11. Lai L-J, Zhu Z-N (2017) Design, modeling and testing of a novel flexure-based displacement amplification mechanism. Sens Actuators A Phys 266:122–129
12. Lobontiu N, Paine JSN, Garcia E, Goldfarb M (2001) Corner-filleted flexure hinges. J Mech Des 123(3):346–352
13. Tian Y, Shirinzadeh B, Zhang D (2010) Closed-form compliance equations of filleted v-shaped flexure hinges for compliant mechanism design. Precis Eng J Int Soc Precis Eng Nanotechnol 34(3):408–418
14. Li LJ, Zhang D, Guo S, Qu HB (2019) Design, modeling, and analysis of hybrid flexure hinges. Mech Mach Theory 131:300–316
15. Qiu L, Yue X, Xie Z (2019) Design and analysis of multicavity flexure hinge (MCFH) based on three-dimensional continuum topology optimization. Mech Mach Theory 139:21–33
16. Zhang XZ, Xu QS (2018) Design and testing of a new 3-dof spatial flexure parallel micropositioning stage. Int J Precis Eng Manuf 19(1):109–118
17. Li L, Zhang D, Guo S, Qu H (2017) A generic compliance modeling method for two-axis elliptical-arc-filleted flexure hinges. Sensors 17(9):66
18. Li ZY, Liu PB, Yan P (2021) Design and analysis of a novel flexure-based dynamically tunable nanopositioner. Micromachines 12(2):13
19. Lin R, Li Y, Zhang Y, Wang T, Wang Z, Song Z, Dou Z, Qian J (2019) Design of a flexure-based mixed-kinematic xy high-precision positioning platform with large range. Mech Mach Theory 142:66
20. Qin Y, Shirinzadeh B, Tian Y, Zhang D (2013) Design issues in a decoupled xy stage: static and dynamics modeling, hysteresis compensation, and tracking control. Sens Actuators A Phys 194:95–105
21. Yang R, Jouaneh M, Schweizer R (1996) Design and characterization of a low-profile micropositioning stage. Precis Eng 18(1):20–29
22. Chapuis D, Gassert R, Sache L, Burdet E, Bleuler H (2004) Design of a simple MRI/fMRI compatible force/torque sensor. In: 2004 IEEE/RSJ international conference on intelligent robots and systems (IROS) (IEEE Cat. No.04CH37566), vol 3, pp 2593–25993.
23. Qin Y, Shirinzadeh B, Zhang D, Tian Y (2013) Compliance modeling and analysis of statically indeterminate symmetric flexure structures. Precis Eng J Int Soc Precis Eng Nanotechnol 37(2):415–424
24. Ma H-W, Yao S-M, Wang L-Q, Zhong Z (2006) Analysis of the displacement amplification ratio of bridge-type flexure hinge. Sens Actuators A Phys 132(2):730–736
25. Yong YK, Lu T-F, Handley DC (2008) Review of circular flexure hinge design equations and derivation of empirical formulations. Precis Eng 32(2):63–70
26. Ling M, Howell LL, Cao J, Chen G (2020) Kinetostatic and dynamic modeling of flexure-based compliant mechanisms: a survey. Appl Mech Rev 72(3):66
27. Valentini PP, Pennestrì E (2017) Second-order approximation pseudo-rigid model of leaf flexure hinge. Mech Mach Theory 116:352–359
28. Liu H (2004) Mechanics of materials, 4th edn. Higher Education Press, Beijing, pp 308–310 **(in Chinese)**
29. Gere JM, Timoshenko SP (1991) Mechanics of materials, 3rd edn. Chaman and Hall, London
30. Yue Y, Gao F, Zhao X, Ge QJ (2010) Relationship among input-force, payload, stiffness and displacement of a 3-dof perpendicular parallel micro-manipulator. Mech Mach Theory 45(5):756–771
31. Qin Y, Shirinzadeh B, Tian Y, Zhang D, Bhagat U (2013) Design and computational optimization of a decoupled 2-dof monolithic mechanism. IEEE/ASME Trans Mechatron 66:872–881
32. Cai K, Tian Y, Wang F, Zhang D, Liu X, Shirinzadeh B (2017) Design and control of a 6-degree-of-freedom precision positioning system. Robot Comput Integr Manuf 44:77–96
33. Wang GG, Shan S (2007) Review of metamodeling techniques in support of engineering design optimization, vol 129, pp 370–380
34. Pham H-H, Chen I-M (2005) Stiffness modeling of flexure parallel mechanism. Precis Eng 29(4):467–478
35. Tian Y, Shirinzadeh B, Zhang D, Liu X, Chetwynd D (2009) Design and forward kinematics of the compliant micro-manipulator with lever mechanisms. Precis Eng 33(4):466–475

Yan-Ding Qin is currently an associate Professor at *College of Artificial Intelligence, Nankai University, Tianjin, China*. He received the Ph.D. degree from *Tianjin University, Tianjin, China*, in 2012. His research interests include micro/nano manipulation robotics, medical robotics, and smart actuators.

Yue-Yang Shi is currently a master candidate at *College of Artificial Intellignece, Nankai University, China*. He received the B.S degree from Chongqing University, Chongqing, China, in 2021.

Bijan Shirinzadeh is currently a professor at *Department of Mechanical and Aerospace Engineering, Monash University, Australia*. He received the Ph.D. degree from *The University of Western Australia, Australia*, in 1990. His research interests include micro/nano manipulation, systems kinematics and dynamics, haptics and robotic-assisted surgery and microsurgery, and advanced manufacturing.

Yan-Ling Tian is currently a professor at *School of Mechanical Engineering, Tianjin University, China*. He received the Ph.D. degree from Tianjin University, China, in 2005. His research interests include micro/nano manipulation, mechanical dynamics, surface metrology and characterization.

Da-Wei Zhang is currently a professor at School of Mechanical Engineering, Tianjin University, China. He received the Ph.D. degree from *Tianjin University, China*, in 1995. His research interests include micro/nano positioning techniques, high speed machining methodologies, and dynamic design of machine tools.